Mechanistic Insight into Peroxydisulfate Reactivity: Oxidation of the cis,cis-[Ru(bpy)$_2$(OH$_2$)]$_2$O^4 "Blue Dimer"

Citation	Hurst, J. K., Roemeling, M. D., & Lymar, S. V. (2015). Mechanistic Insight into Peroxydisulfate Reactivity: Oxidation of the cis, cis-[Ru (bpy)$_2$(OH$_2$)]$_2$O^4 "Blue Dimer". The Journal of Physical Chemistry B, 119(24), 7749-7760. doi:10.1021/acs.jpcb.5b00922
DOI	10.1021/acs.jpcb.5b00922
Publisher	American Chemical Society
Version	Version of Record
Terms of Use	http://cdss.library.oregonstate.edu/sa-termsofuse

THE JOURNAL OF PHYSICAL CHEMISTRY B

Article

pubs.acs.org/JPCB

Mechanistic Insight into Peroxydisulfate Reactivity: Oxidation of the *cis,cis*-$[Ru(bpy)_2(OH_2)]_2O^{4+}$ "Blue Dimer"

James K. Hurst,[†] Margo D. Roemeling,[‡] and Sergei V. Lymar*,[§]

[†]Department of Chemistry, Washington State University, Pullman, Washington 99164, United States

[‡]Department of Biochemistry and Biophysics, Oregon State University, Corvallis, Oregon 97331, United States

[§]Chemistry Department, Brookhaven National Laboratory, Upton, New York 11973, United States

Supporting Information

ABSTRACT: One-electron oxidation of the μ-oxo dimer (*cis,cis*-$[Ru^{III}(bpy)_2(OH_2)]_2O^{4+}$, **{3,3}**) to **{3,4}** by $S_2O_8^{2-}$ can be described by three concurrent reaction pathways corresponding to the three protic forms of **{3,3}**. Free energy correlations of the rate constants, transient species dynamics determined by pulse radiolysis, and medium and temperature dependencies of the alkaline pathway all suggest that the rate-determining step in these reactions is a strongly nonadiabatic dissociative electron transfer within a precursor ion pair leading to the $\{3,4\}|SO_4^{2-}|SO_4^{\bullet-}$ ion triple. As deduced from the $SO_4^{\bullet-}$ scavenging experiments with 2-propanol, the $SO_4^{\bullet-}$ radical then either oxidizes **{3,4}** to **{4,4}** within the ion triple, effecting a net two-electron oxidation of **{3,3}**, or escapes in solution with ~25% probability to react with additional **{3,3}** and **{3,4}**, that is, effecting sequential one-electron oxidations. The reaction model presented also invokes rapid **{3,3}** + **{4,4}** → 2**{3,4}** comproportionation, for which k_{com} ~5×10^7 M^{-1} s^{-1} was independently measured. The model provides an explanation for the observation that, despite favorable energetics, no oxidation beyond the **{3,4}** state was detected. The indiscriminate nature of oxidation by $SO_4^{\bullet-}$ indicates that its fate must be quantitatively determined when using $S_2O_8^{2-}$ as an oxidant.

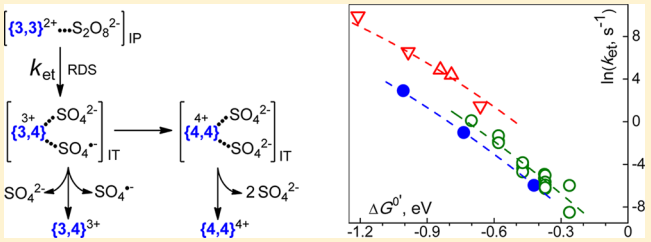

INTRODUCTION

The peroxydisulfate anion ($S_2O_8^{2-}$) is a powerful oxidant ($E^0(S_2O_8^{2-}/2SO_4^{2-})$ = 1.94 V) that has been extensively used to study electron transfer reactions of coordination compounds[1−10] and as a terminal electron acceptor in photocatalyzed redox reactions.[11−24] The underlying mechanisms of these reactions are not straightforward, however, because one-electron reduction of $S_2O_8^{2-}$ generates the sulfate radical anion, which is a yet more powerful and less discriminant oxidant than $S_2O_8^{2-}$ itself (i.e., $E^0(SO_4^{\bullet-}/SO_4^{2-})$ = 2.44 V).[25] One-electron reduction of $S_2O_8^{2-}$ to form $SO_4^{\bullet-}$ is correspondingly less favorable ($E^0(S_2O_8^{2-}/SO_4^{\bullet-},SO_4^{2-})$ = 1.45 V). As a consequence, stoichiometries and pathways of noncomplementary reactions can be sensitive to the reductant energetics and the composition of the reaction medium. For example, a detailed study of the reaction between $S_2O_8^{2-}$ and the binuclear pyrazine (pz)-bridged $Ru_2(NH_3)_{10}pz^{4+}$ ion led Fürholz and Haim to conclude that both one-electron and two-electron oxidations had occurred.[5] A common mechanism was proposed that involved formation of a reactive ion pair; following the initial electron transfer step, the caged product complex that was generated ($Ru_2(NH_3)_{10}pz^{5+}|SO_4^{\bullet-},SO_4^{2-}$) either underwent a rapid second electron transfer step to give the two-electron product, $Ru_2(NH_3)_{10}pz^{6+}$, or cage escape ensued leading to generation of free $SO_4^{\bullet-}$ and, ultimately, formation of a second one-electron product, $Ru_2(NH_3)_{10}pz^{5+}$. Thus, the product distribution depended upon how the caged intermediate partitioned between its decay channels. One-electron oxidation of the water oxidation catalyst, $[Ru^{III}L_2(OH_2)]_2O^n$ (L = 2,2′-bipyridyl-4,4′-dicarboxylate), to the corresponding mixed-valent (**{3,4}**) ion has also been noted,[12] although this reaction was not extensively investigated. (The notations **{3,3}**, **{3,4}**, etc., are intended to indicate *formal* oxidation states of the metal centers only; they identify the overall level of oxidation without implying the actual electron distribution.)

In this study, we describe in greater detail the oxidation kinetics of the underivatized analogue, $[Ru^{III}(bpy)_2(OH_2)]_2O^{4+}$ (bpy = 2,2′-bipyridine), whose overall electrostatic charge and redox thermodynamics are better defined than the dicarboxy-substituted complex ion. The presence of aqua ligands in this class of compounds permits thermodynamic access to higher oxidation states via redox-leveling deprotonation steps.[26]

One curious feature of these reactions is that oxidation to **{5,5}** is thermodynamically feasible, i.e., the reaction $\{3,3\}^{n+}$ + $2S_2O_8^{2-}$ → **{5,5}** + $2SO_4^{2-}$ + nH^+ (n = 2−4) is exergonic (by ~0.6−1.3 V over the pH range 0−14), yet oxidation proceeds only to the **{3,4}** state, as will later be shown. Access to the **{5,5}** state is of particular interest because it leads to spontaneous

Special Issue: John R. Miller and Marshall D. Newton Festschrift

Received: January 28, 2015
Revised: March 22, 2015
Published: March 27, 2015

DOI: 10.1021/acs.jpcb.5b00922
J. Phys. Chem. B 2015, 119, 7749−7760

oxidation of water to O_2.[27,28] Thus, although these dimers are potentially capable of catalyzing water oxidation by peroxydisulfate, this is not observed. In this study, we make extensive use of pulse radiolysis and recently estimated one-electron reduction potentials for the higher oxidation states of the "blue dimer"[27,29,30] to arrive at an explanation for its unusual chemical reactivity.

EXPERIMENTAL SECTION

Materials. The ruthenium dimer, *cis,cis*-[Ru(bpy)$_2$(OH$_2$)]$_2$O^{4+}, was prepared from *cis*-Ru(bpy)$_2$Cl$_2$, isolated as the perchlorate salt, and characterized as previously described.[27] Reactant solution concentrations were determined spectrophotometrically using $\varepsilon_{636} = 2.2 \times 10^4$ M^{-1} cm^{-1} for {**3,3**} in acidic media[27] as a reference value for determining molar extinction coefficients under other medium conditions and for other oxidation states. Solutions of {**3,4**} were prepared from {**3,3**} by oxidation with $K_2S_2O_8$. Trifluoromethanesulfonic (triflic) acid (HOTf) obtained from TCI America was twice redistilled under a vacuum and stored at 4 °C as a 1 M solution. Potassium peroxydisulfate, buffers, and other chemicals were best-available grade from commercial suppliers and were used as received. Milli-Q purified (ASTM type I) water was used throughout. Buffers and electrolytes added to adjust ionic strength utilized sodium salts so that, although K^+ was introduced with $K_2S_2O_8$, the predominant cation in the reaction solutions was Na^+.

Methods. Optical spectra were recorded using HP 8452 Diode Array or Cary 500 spectrophotometers. Kinetic measurements of thermal reactions were made using an Applied Photophysics SX18MV-R stopped-flow instrument equipped with a thermostatting water bath and both conventional PMT and photodiode array detectors.

The majority of pulse radiolysis experiments were carried out with 2 MeV electrons from a Van de Graaff accelerator; pulse widths were in the range 0.08−0.25 μs, and a 2 cm long quartz flow cell was used in the detection optical path. The sample solutions were prepared in situ by flow-mixing the desired components using a remotely controlled syringe pump, as shown in Figure S1 (Supporting Information). The radiation pulse and optical kinetics detection were timed to occur either shortly after mixing or while the solution was still flowing. The analyzing Xe-arc light source was pulsed for kinetics recorded on time scales of less than 100 μs. All experiments were done with temperature stabilization at 25 ± 0.5 °C. The radiation yields of radicals (G-values) are given in number of radicals per 100 eV absorbed energy. Dosimetry was performed with a N_2O-saturated 10 mM KSCN solution using $G\varepsilon = 4.87 \times 10^4$ ions (100 eV)$^{-1}$ M^{-1} cm^{-1} for the $(SCN)_2^{\bullet-}$ radical at 472 nm.

Pulse radiolysis with subnanosecond temporal resolution was carried out with 9 MeV electrons at the BNL Laser Electron Accelerator Facility (LEAF). A ~30 ps radiation pulse was applied to all samples. The monitoring light source was a pulsed 75 W Xe-arc lamp. Probe wavelengths were selected using 10 nm bandpass interference filters, and the transient absorption signals were detected with a biplanar phototube and digitized at a 20 GS/s rate.

Kinetic analysis was carried out with the in-house developed INTKIN software. This program uses numerical integration of rate equations to produce time−concentration and time−absorbance data for all least-squares analyses.

RESULTS

Stoichiometry. Addition of excess $S_2O_8^{2}$ to a solution of {**3,3**} resulted in decay of its characteristic absorption in the 600−650 nm region and the appearance of a new absorption band in the 480−500 nm region attributable to formation of {**3,4**}.[27,29] As shown in Figure 1, these changes occur with two

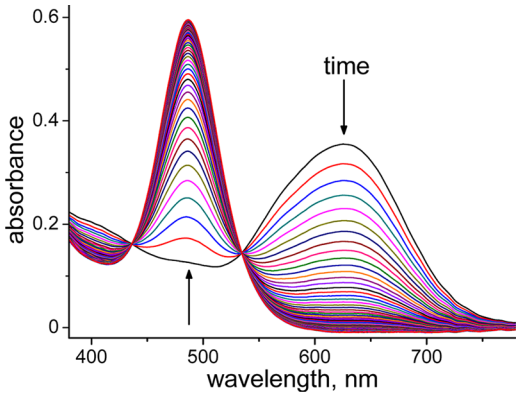

Figure 1. Absorption traces recorded every 50 ms over 5 s upon flow mixing of 20 mM $S_2O_8^{2-}$ in water and 52 μM {**3,3**} in 20 mM borate at pH 9.2 and 25 °C; the ionic strength of the mixed solution was 35 mM.

well-defined isosbestic points in the visible−near IR range, which indicates the constancy of reaction stoichiometry over the entire reaction time. Thus, the reaction is n{**3,3**} + $S_2O_8^{2-}$ → products.

The reaction stoichiometry with respect of the {**3,3**} consumption (n value) can be established by using an excess of {**3,3**} over $S_2O_8^{2-}$, as shown in Figure 2 (solid traces). Under

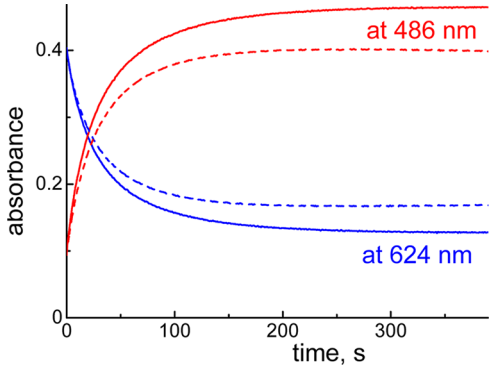

Figure 2. Kinetics of the {**3,3**} absorption decay recorded at 624 nm (blue) and the {**3,4**} absorption growth recorded at 486 nm (red) in a N_2-purged solution containing 135 μM {**3,3**} and 45 μM $S_2O_8^{2-}$ without (solid traces) and with 125 mM 2-propanol (dashed traces) at pH 11 (NaOH) and 25 °C. Optical path 2 mm.

these conditions, consumption of {**3,3**} is incomplete and the absorbance change at 624 nm (ΔA) is related to the concentration of added $[S_2O_8^{2-}]_0$ by $\Delta A = n(\varepsilon_{33} - \varepsilon_p)[S_2O_8^{2-}]_0$. At pH 11, the molar absorptivity of {**3,3**} at 624 nm is $\varepsilon_{33} = 1.5 \times 10^4$ M^{-1} cm^{-1} and the molar absorptivity of products ($\varepsilon_p = 230$ M^{-1} cm^{-1}) has been obtained from the final spectrum in experiments with $S_2O_8^{2-}$ in excess of {**3,3**}. Using these values and the data in Figure 2, we obtain $n = 2.06$. Thus, the reaction stoichiometry closely corresponds to

$$2\{\mathbf{3,3}\} + S_2O_8^{2-} \rightarrow 2\{\mathbf{3,4}\} + 2SO_4^{2-} \quad (1)$$

DOI: 10.1021/acs.jpcb.5b00922
J. Phys. Chem. B 2015, 119, 7749−7760

in accordance with $S_2O_8^{2-}$ acting as a net two-electron oxidant. This stoichiometry was confirmed in titrimetric experiments where aliquots of $K_2S_2O_8$ were added sequentially to pH 9.2 borate solutions containing (initially) excess {3,3} and the extent of oxidation to {3,4} was determined spectrophotometrically (Figure S2, Supporting Information).

Kinetics. Preliminary experiments had shown that below pH ~9 the rate of reaction 1 decreased progressively with increasing acidity. This behavior can be attributed to differing reactivity of the various protonation states of the dimer (discussed below). The alkaline pathway was chosen for rigorous kinetic analysis because it could be easily isolated, thereby obviating complications arising from contributions from parallel reaction channels, and because reactions in the neutral region were not kinetically well-behaved (as described below).

Above pH 9 with $S_2O_8^{2-}$ in excess, the decay of {3,3} was rigorously exponential with the observed rate constant proportional to $[S_2O_8^{2-}]$ (Figure 3). The corresponding rate law is therefore

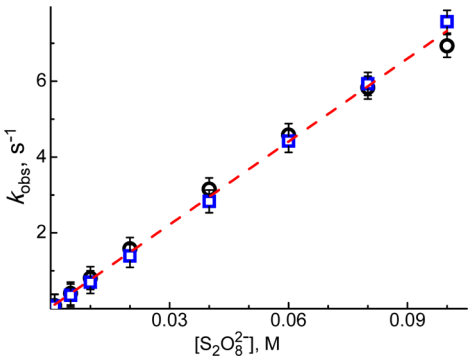

Figure 3. Dependence of the observed first-order rate constant of {3,3} oxidation (k_{obs}) upon the concentration of $S_2O_8^{2-}$ taken in excess over $[\{3,3\}]_0$ = 46.5 μM at pH 11 (NaOH), 25 °C, and constant ionic strength of 0.3 M maintained with NaOTf (circles) or $NaClO_4$ (squares). The dashed line shows the linear fit to all data that gives a slope of 73 ± 1 M^{-1} s^{-1}.

$$-\frac{d[\{3,3\}]}{dt} = k_{obs}[\{3,3\}] = k_{app}[\{3,3\}][S_2O_8^{2-}] \quad (2)$$

where k_{app} is the apparent bimolecular rate constant. Since {3,3} carries a 2+ charge above pH 9, k_{obs} exhibits a strong ionic strength dependence, as shown in Figure 4.

A simple treatment of this ionic strength dependence according to the semiempirical Davies equation

$$\log k_{obs} = \log k^0_{obs} + 1.02Z_AZ_B\left(\frac{\sqrt{\mu}}{1+\sqrt{\mu}} - 0.3\mu\right) \quad (3)$$

gives a reasonably straight line corresponding to $k^0_{app} = k^0_{obs}/[S_2O_8^{2-}] = 910 \pm 70$ M^{-1} s^{-1} and the product of reactant charges $Z_AZ_B = -3.9 \pm 0.2$ (Figure 4, up triangles); the latter is close to the expected value of −4. A slightly better linearization can be obtained using the extended Debye–Hückel equation

$$\log k_{obs} = \log k^0_{obs} + 1.02Z_AZ_B\left(\frac{\sqrt{\mu}}{1+0.328r_0\sqrt{\mu}}\right) \quad (4)$$

with the closest center-to-center approach of ions (considered spherical) r_0 = 6 Å. Again, the slope $Z_AZ_B = -3.92 \pm 0.06$ (Figure 4, down triangles) is very close to −4 and the zero-ionic strength value of the apparent second-order rate constant $k^0_{app} = k^0_{obs}/[S_2O_8^{2-}] = 880 \pm 20$ M^{-1} s^{-1}.

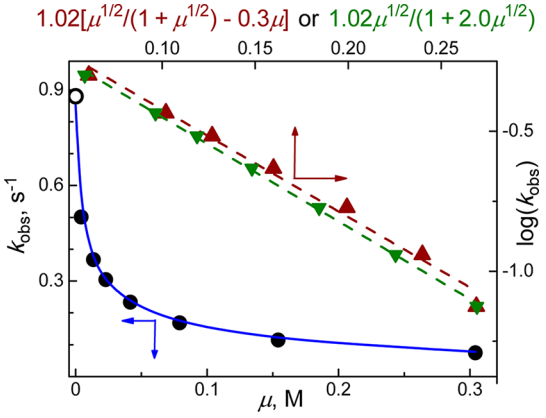

Figure 4. Left-bottom axes: dependence of the observed first-order rate constant for {3,3} oxidation (k_{obs}) upon ionic strength maintained with NaOTf (solid circles); the open circle shows k^0_{obs} = 0.88 s^{-1} obtained from data extrapolation to zero ionic strength. Conditions: $[S_2O_8^{2-}]$ = 1 mM, [{3,3}] = 28 μM, pH 11 (NaOH), 25 °C. The blue line shows modeling results to eqs 5–7 as described in the text. Right-top axes: logarithmic data representations and their linear fits according to Davies (eq 3, up triangles, slope = −3.9 ± 0.2, and intercept = −0.039 ± 0.033) and extended Debye–Hückel (eq 4, down triangles, slope = −3.9 ± 0.1, and intercept = −0.058 ± 0.009).

A general mechanism that accounts for both the observed stoichiometry and rate law is shown in Scheme 1. As with any bimolecular reaction, formation of a precursor complex between {3,3} and $S_2O_8^{2-}$ precedes the rate-determining step (RDS). This complex can be viewed as an ion pair undergoing either one-electron transfer producing {3,4} and sulfate free radical (k_{et1} pathway) or two-electron transfer producing {4,4} as the intermediate (k_{et2} pathway). The {4,4} intermediate and/or $SO_4^{\bullet-}$ radical produced in the RDS subsequently engage in rapid redox reactions, as shown in Scheme 1, that result in the observed overall reaction 1 stoichiometry.

Scheme 1

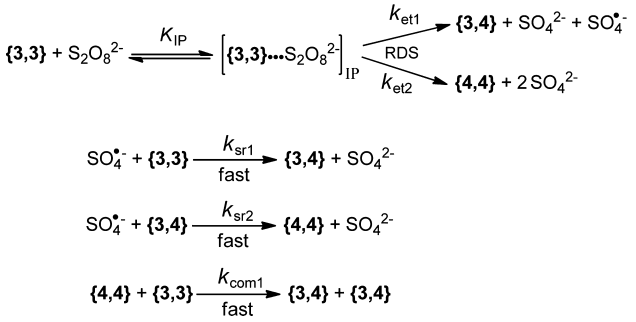

With $S_2O_8^{2-}$ in excess, Scheme 1 leads to the following expression for the observed rate constant

$$k_{obs} = 2k_{et}\frac{K_{IP}[S_2O_8^{2-}]}{1 + K_{IP}[S_2O_8^{2-}]} \quad (5)$$

where $k_{et} = k_{et1} + k_{et2}$. The absence of downward curvature in Figure 3 indicates that the K_{IP} value is so small that $1 \gg K_{IP}[S_2O_8^{2-}]$ even at 0.1 M peroxydisulfate. Under these limiting conditions, eq 5 reduces to $k_{obs} = 2k_{et}K_{IP}[S_2O_8^{2-}]$. Within this

DOI: 10.1021/acs.jpcb.5b00922
J. Phys. Chem. B 2015, 119, 7749–7760

formalism, the ionic strength dependence shown in Figure 4 is controlled primarily by K_{IP} because in alkaline solution the ion pair is uncharged. The Debye−Hückel treatment of ion pairing with the center-to-center separation of spherical reactants between r_0 and $r_0 + \delta r$ has led to the following equations[31,32]

$$K_{IP} = \frac{4\pi L r_0^2 \delta r}{1000} \exp\left(-\frac{W(r_0)}{kT}\right) \quad (6)$$

$$W(r_0) = \frac{Z_A Z_B e^2}{D r_0(1 + \kappa r_0)} \quad \text{and} \quad \kappa = \sqrt{\frac{8\pi L e^2}{1000 DkT}\mu} \quad (7)$$

Here, L is the Avogadro number, e is the electron charge, D is the bulk dielectric constant of water, and the other symbols have their usual meanings. The only parameters in eqs 5−7 that are not accurately known are r_0, δr, and k_{et}, although only the $k_{et}\delta r$ product is needed for describing the k_{obs} vs μ dependence. By setting r_0 = 6 Å (the same value as used in eq 4) and treating the $k_{et}\delta r$ product in eqs 5−7 as the only adjustable parameter, a good fit to the data has been obtained with $k_{et}\delta r$ = 16 Å s^{-1} at 25 °C (Figure 4, blue curve). If we accept $\delta r \approx 1$ Å, a typical value,[33] we can estimate $k_{et} \approx 16$ s^{-1}.

Another popular expression for K_{IP} suggested by Fuoss[34] can be obtained from eq 6 by setting $\delta r = r_0/3$. The so-modified equation fits the data equally well with the same r_0 = 6 Å but with k_{et} decreased by a factor of ~2 to $k_{et} \approx 8$ s^{-1}. Notably, eq 6 with r_0 = 6 and δr_0 = 1 Å gives K_{IP} = 2.6 M^{-1} at μ = 0.3 M, and from the Fuoss equation K_{IP} = 5.2 M^{-1} with the same μ and r_0; thus, the $K_{IP}[S_2O_8^{2-}]$ product remains sufficiently small for all data points in Figure 3 that the downward deviation from linearity is not detectable. Attempts to use r_0 values outside the 5−7 Å limits have led to significant deviations of slopes $Z_A Z_B$ in the extended Debye−Hückel equation (eq 4) from their expected value of −4; moreover, no acceptable fits of eqs 5−7 to the k_{obs} vs μ dependence in Figure 4 could be obtained with r_0 values outside these margins. Thus, we estimate $r_0 = 6 \pm 1$ Å.

Whereas eqs 4, 6, and 7 are derived under assumption of spherical reactants, a regular shape that better describes the $S_2O_8^{2-}$ ion is a prolate spheroid;[35] similarly, the shape of the ruthenium dimer approximates that of a hemiellipsoidal segment of a spheroid.[29] Accordingly, r_0 can be roughly taken as equal to the sum of radii of equivalent spheres with volumes equal to the reactants' estimated volumes. Applying this procedure, we obtain r_0 = 1.9 + 5.2 = 7.1 Å, where the first and second terms are the equivalent radii of $S_2O_8^{2-}$ and **{3,3}**, respectively (see the Supporting Information for calculational details). This r_0 estimate is only 20% larger than the value of 6 Å obtained from the experimental data.

The alkaline reaction is significantly activated, and the corresponding Arrhenius parameters derived from the temperature dependence in Figure 5 are $A = (4.5 \pm 0.3) \times 10^8$ M^{-1} s^{-1} and E_a = 8.11 ± 0.05 kcal/mol. In terms of Scheme 1, the activated complex formalism, and eq 5, the apparent bimolecular rate constant is

$$k_{app} = 2K_{IP}k_{et} = 2\frac{RT}{Lh} \exp\left(\frac{\Delta_{IP}S + \Delta_{et}S^{\#}}{R}\right) \exp\left(-\frac{\Delta_{IP}H + \Delta_{et}H^{\#}}{RT}\right) \quad (8)$$

In this equation, $\Delta_{IP}S$ and $\Delta_{IP}H$ are the entropy and enthalpy associated with ion pairing and $\Delta_{et}S^{\#}$ and $\Delta_{et}H^{\#}$ are the corresponding activation parameters for the electron transfer step; the steric factor and transmission coefficient for this step are both rolled into the $\Delta_{et}S^{\#}$ term. From the Arrhenius parameters, we obtain for the apparent activation entropy $\Delta S_{app}^{\#} = R \ln 2 + \Delta_{IP}S + \Delta_{et}S^{\#} = -20.9 \pm 0.2$ e.u. and for the enthalpy $\Delta H_{app}^{\#} = \Delta_{IP}H + \Delta_{et}H^{\#} = 7.52 \pm 0.04$ kcal/mol.

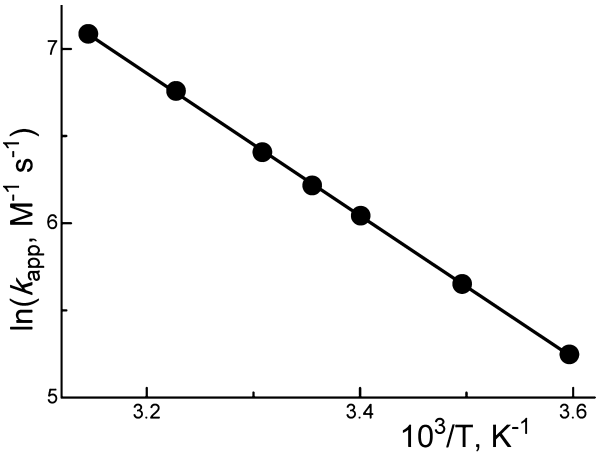

Figure 5. Temperature dependence in Arrhenius coordinates of the apparent second-order rate constant for **{3,3}** oxidation (circles) and its linear fit. Conditions: $[S_2O_8^{2-}]$ = 1 mM, [**{3,3}**] = 28 μM, pH 11 (NaOH), μ = 0.004 M.

Within the model given by eqs 6 and 7, the entropy of ion pairing is

$$\Delta_{IP}S = R\frac{\partial(T \ln K_{IP})}{\partial T} = R \ln\left(\frac{4\pi L r_0^2 \delta r}{1000}\right) + \frac{W(r_0)}{T}\left[\left(1 - \frac{\kappa r_0}{2(1 + \kappa r_0)}\right)\frac{T}{D}\frac{\partial D}{\partial T} - \frac{\kappa r_0}{2(1 + \kappa r_0)}\right] \quad (9)$$

The first right-hand term in this equation is associated with the restriction on the reactants' translational motion in the ion pair and is therefore negative; with r_0 = 6 and δr_0 = 1 Å, this term is −2.6 e.u. This negative contribution is more than compensated by the second, electrostatic right-hand term which is positive and amounts to 10.9 e.u.; this number has been computed using $\partial D/\partial T$ = −0.36 K^{-1} at 25 °C[36] and μ = 0.004 M as in Figure 5. The positive electrostatic contribution to the ion pairing entropy is expected because the ordering of solvent around an ion pair is greatly reduced due to charge neutralization (in this case, the ion pair has zero charge) compared to stronger ordering around the free individual ions. Thus, $\Delta_{IP}S \approx 8.3$ e.u. and the activation entropy for the rate limiting electron transfer step is even more negative than $\Delta S_{app}^{\#}$, that is, $\Delta_{et}S^{\#} \approx -30.6$ e.u. Despite the Coulombic attraction of the oppositely charged reactants, the enthalpy of ion pairing is slightly positive and amounts to $\Delta_{IP}H = -RT \ln K_{IP} - T\Delta_{IP}S \approx 0.8$ kcal/mol, which indicates that the ion pairing is driven predominantly by the entropy increase. The activation enthalpy for electron transfer is thus $\Delta_{et}H^{\#} \approx 6.7$ kcal/mol.

As the solution is acidified, the specific rate of **{3,3}** oxidation by $S_2O_8^{2-}$ falls off the plateau observed in alkaline solutions, reaching a much lower plateau in acidic media (Figure 6). Whereas in both alkaline and acidic media with $S_2O_8^{2-}$ in excess, **{3,3}** decay kinetics were rigorously exponential, in neutral

DOI: 10.1021/acs.jpcb.5b00922
J. Phys. Chem. B 2015, 119, 7749−7760

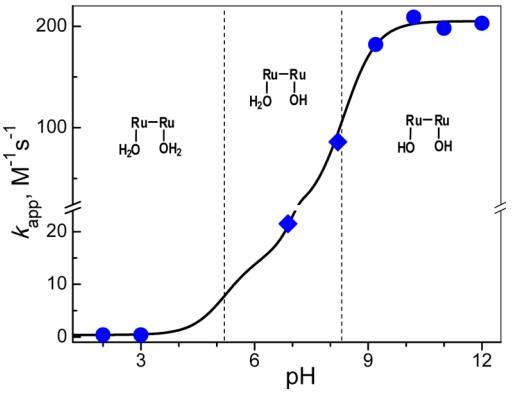

Figure 6. pH dependence of the apparent bimolecular rate constant for {3,3} oxidation (k_{app}) measured at 25 °C and constant [{3,3}] = 20 μM, [$S_2O_8^{2-}$] = 10 mM, and μ = 40 mM maintained with $NaClO_4$. NaOH (pH 11 and 12), borate buffer (8 < pH < 11), phosphate buffer (pH 6.9), and $HClO_4$ (pH 2 and 3) were used to control pH. Circles mark data obtained from fitting the entire {3,3} exponential decay kinetics, and diamonds indicate data derived from the initial {3,3} decay rates. The solid line corresponds to eq 10 with k_1 = 0.4, k_2 = 15, and k_3 = 200 M^{-1} s^{-1}, and with pK_{a1} = 5.2 and pK_{a2} = 8.3. The dashed vertical lines separate the predominance domains for various protonation states of {3,3}. Note the vertical axis break.

media, significant deviations from exponentiality were observed (Figure S3, Supporting Information). We therefore derived the k_{app} values in the neutral region from the initial {3,3} decay rates. The pH dependence in Figure 6 is associated with two protic equilibria involving the water ligands of {3,3} that occur with pK_{a1} ≈ 5 and pK_{a2} ≈ 8 (see Table S1, Supporting Information), which leads to the following expression for the apparent bimolecular rate constant (as defined by eq 2)

$$k_{app} = \frac{k_1[H^+]^2 + k_2K_{a1}[H^+] + k_3K_{a1}K_{a2}}{[H^+]^2 + K_{a1}[H^+] + K_{a1}K_{a2}} \quad (10)$$

where k_1, k_2, and k_3 are the rate constants for fully protonated, singly deprotonated, and doubly deprotonated {3,3} species, respectively. Figure 6 shows that the observed pH dependence can be satisfactorily reproduced by eq 10 and that the rate constant increases by a factor of 20 upon dissociation of the first proton and another factor of 10 upon dissociation of the second proton. This increase occurs despite the decrease in ion pairing between {3,3} and $S_2O_8^{2-}$ due to the decrease in the positive charge on {3,3}. The K_{IP} values at μ = 40 mM evaluated through eqs 6 and 7 are 8, 42, and 220 M^{-1} for the alkaline, neutral, and acidic regions, respectively, in Figure 6. Using these values, the rate constants k_1–k_3, derived from Figure 6, and eq 5, we estimate that the electron transfer rate constant (k_{et}, Scheme 1) increases from ~1 × 10^{-3} to ~0.25 and to ~13 s^{-1} upon going from fully protonated to singly deprotonated and to doubly deprotonated {3,3} species.

Radical Scavenging. To investigate the conjecture in Scheme 1 that the intermediacy of free $SO_4^{\bullet-}$ radical plays a role in the overall oxidation process, we have examined the effect of a radical scavenger, 2-propanol (2-PrOH), on the reaction rate and yield. In the presence of 2-PrOH, a portion of the $SO_4^{\bullet-}$ radical will be converted into the carbon-centered alcohol radical[37]

$$SO_4^{\bullet-} + (CH_3)_2C(H)OH \rightarrow HSO_4^- + (CH_3)_2{}^{\bullet}COH$$
$$k_{sc} = (3–9) \times 10^7\ M^{-1}\ s^{-1} \quad (11)$$

This strongly reducing radical, $E^0((CH_3)_2CO,H^+/(CH_3)_2{}^{\bullet}COH) = -1.39$ V,[38] will rapidly reduce the blue dimer in all oxidation states involved in Scheme 1. The most consequential reactions brought about by $SO_4^{\bullet-}$ radical scavenging are summarized in Scheme 2.

Scheme 2

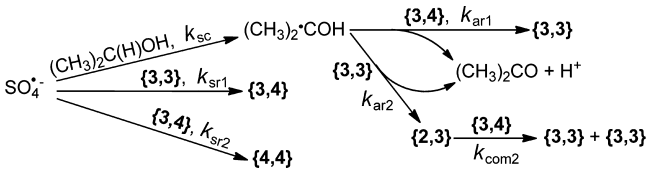

If we designate the $SO_4^{\bullet-}$ radical yield in Scheme 1 as $\alpha = k_{et1}/(k_{et1} + k_{et2})$ and the scavenging efficiency in Scheme 2 as $\beta = k_{sc}[2\text{-PrOH}]/(k_{sc}[2\text{-PrOH}] + k_{sr1}[\{3,3\}] + k_{sr2}[\{3,4\}])$, the instantaneous yield of {3,3} oxidation by $S_2O_8^{2-}$ in the presence of 2-PrOH becomes

$$Y_t = -\frac{d[\{3,3\}]}{d[S_2O_8^{2-}]} = 2(1 - \alpha\beta) \quad (12)$$

Implicit in this equation is the assumption of low steady-state concentrations for all intermediates (both radicals, {2,3}, and {4,4}), which allows us to neglect their cross reactions, disproportionation, and radical self-recombination. Other simplifications arise from the facts that $k_{sr1} \approx k_{sr2} = k_{sr}$, as will be described in the next section, and that [{3,3}] + [{3,4}] ≈ [{3,3}]$_0$, the concentration of added blue dimer. We thus write β = [2-PrOH]/([2-PrOH] + γ), where $\gamma = k_{sr}[\{3,3\}]_0/k_{sc}$ is a time-independent parameter, and obtain for the integral yield

$$Y_{int} = -\frac{\Delta[\{3,3\}]}{\Delta[S_2O_8^{2-}]} = 2\left(1 - \alpha\frac{[2\text{-PrOH}]}{[2\text{-PrOH}] + \gamma}\right) \quad (13)$$

Tests of this equation are presented in Figures 2 and 7a, where the integral {3,3} oxidation yield is measured with {3,3} in excess over $S_2O_8^{2-}$. These experiments were performed under strictly anaerobic conditions to avoid complications arising from rapid addition of dissolved oxygen to $(CH_3)_2{}^{\bullet}COH$ to form a peroxy radical. As can be observed in Figure 2, addition of 2-PrOH does decrease the magnitudes of both the {3,3} absorption decay and {3,4} absorption growth. The 2-PrOH concentration dependence of this effect in Figure 7a is consistent with eq 13, provided that $\alpha \approx 0.25$ and $\gamma \approx 0.05$ M. The latter parameter is within the range 0.02–0.07 M calculated from $k_{sr} \approx 1.5 \times 10^{10}\ M^{-1}\ s^{-1}$ (next section), [{3,3}]$_0$, and k_{sc} literature values for reaction 11.

Schemes 1 and 2 predict that oxidation of {3,3} to {3,4} should go to completion in sufficient excess of $S_2O_8^{2-}$ despite partial consumption of $S_2O_8^{2-}$ toward oxidation of 2-PrOH to acetone. As shown in Figure 7b, this has indeed been observed, but the reaction rate is markedly decreased by the addition of 2-PrOH. Assuming that 0.5 M 2-PrOH is sufficient to scavenge all $SO_4^{\bullet-}$ radicals, we identify the rate constants for dashed traces in Figure 7b as $2k_{et2}$ = 1.3 s^{-1} and the solid traces as $2(k_{et1} + k_{et2})$ = 1.7 s^{-1}, from which α = 0.24, in agreement with the value derived from the yield data in Figure 7a. We thus conclude that the partitioning between the two-electron pathway and one-electron free radical pathway in Scheme 1 is ~3:1.

Pulse Radiolysis. This technique has been used to investigate several individual reactions involved in Schemes 1 and 2. Previously, we had determined the rate constant k_{sr2} = 1.5

DOI: 10.1021/acs.jpcb.5b00922
J. Phys. Chem. B 2015, 119, 7749–7760

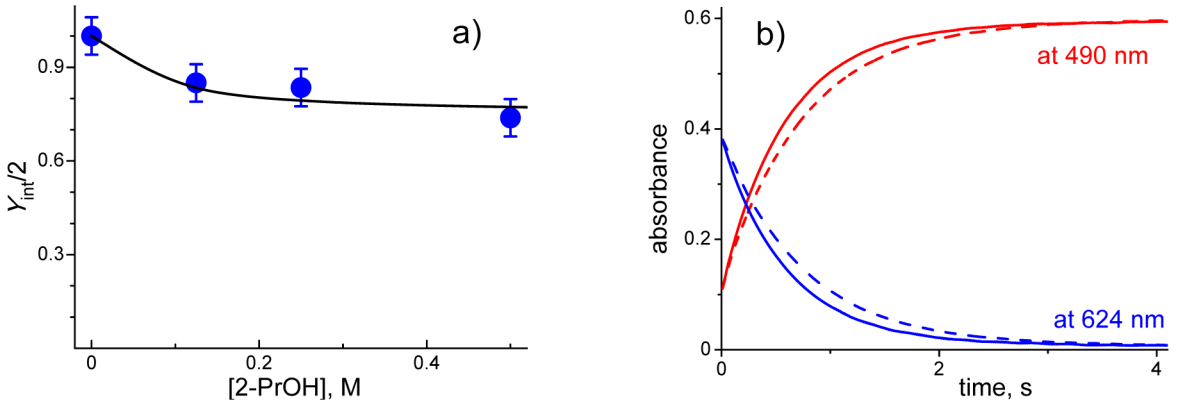

Figure 7. Effect of added 2-PrOH on the {3,3} + $S_2O_8^{2-}$ reaction in a N_2-purged solution at 25 °C. (a) Integral yield, Y_{int}, of {3,3} to {3,4} conversion under the conditions of Figure 2, that is, with ~1.5 stoichiometric excess of {3,3} over $S_2O_8^{2-}$. The yield is defined in eq 13, and the solid line shows the fit to this equation with $\alpha = 0.25$ and $\gamma = 0.05$ M. (b) Kinetics of {3,3} to {3,4} conversion recorded at 624 nm (decay of {3,3}, blue traces) and 490 nm (accumulation of {3,4}, red traces) under a large excess of $S_2O_8^{2-}$ (10 mM) over {3,3} (26 μM) in 10 mM borate at pH 9.2. Solid and dashed lines show the data without and with 0.5 M 2-PrOH, respectively. All traces can be fitted very well to single exponential kinetics with pseudo-first-order rate constants of 1.7 s^{-1} (2-PrOH absent) and 1.3 s^{-1} (2-PrOH present).

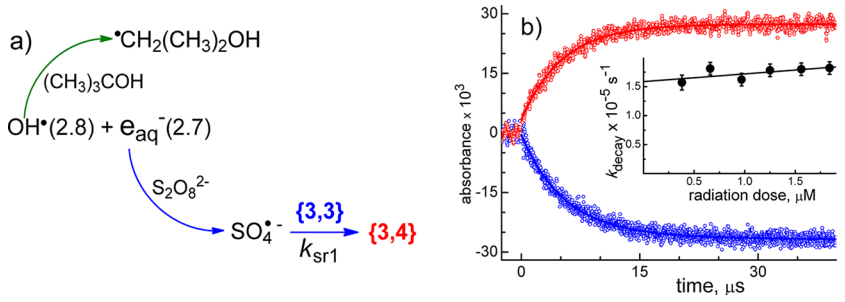

Figure 8. (a) Experimental design for measuring k_{sr1}. Green and blue arrows represent reactions initiated by the hydroxyl radical and hydrated electron, respectively. Numbers in parentheses represent radiation yields (*G*-values) for these pathways. (b) Kinetics of the {3,3} + $SO_4^{\bullet-}$ reaction recorded at 630 nm (blue, {3,3} decay) and 490 nm (red, {3,4} formation). Two Ar-purged buffered (2 mM borate, pH 9.2, plus 10 mM *tert*-butyl alcohol) solutions, one containing 20 μM {3,3} and the other containing 4 mM $S_2O_8^{2-}$, are 1:1 flow-mixed and passed through an optical flow cell using a remotely controlled syringe pump (Figure S1, Supporting Information). Pulse radiolysis and detection are timed to occur while the solutions are still flowing. The lines show exponential fits to the data with the rate constants 1.8×10^5 s^{-1} (blue) and 1.9×10^5 s^{-1} (red). The inset shows the dependence of the {3,3} decay rate constant on the radiation dose expressed as concentration per unit radiation yield, and the line gives a linear fit with the intercept of 1.6×10^5 s^{-1}.

$\times 10^{10}$ M^{-1} s^{-1} at pH 7.2 and μ = 11 mM.[30,39] The $SO_4^{\bullet-}$ radical was generated in Ar-purged solutions containing $S_2O_8^{2-}$ and *tert*-butanol. Under these conditions, the major primary radicals from water radiolysis, the hydrated electron and hydroxyl, were scavenged on sub-microsecond time scales, as follows[40]

$$S_2O_8^{2-} + e_{aq}^- \rightarrow SO_4^{2-} + SO_4^{\bullet-} \quad k_{14} = 1.2 \times 10^{10}\ M^{-1}\ s^{-1} \tag{14}$$

$$(CH_3)_3COH + OH^{\bullet} \rightarrow {}^{\bullet}CH_2C(CH_3)_2OH + H_2O \quad k_{15} = 6.0 \times 10^8\ M^{-1}\ s^{-1} \tag{15}$$

Control experiments conducted in N_2O-saturated solutions (~25 mM N_2O), where e_{aq}^- is converted to $OH^{\bullet}$

$$N_2O + e_{aq}^-(+H_2O) \rightarrow N_2 + OH^- + OH^{\bullet} \quad k_5 = 9.1 \times 10^9\ M^{-1}\ s^{-1} \tag{16}$$

and the $SO_4^{\bullet-}$ radical is not produced, demonstrated that the ${}^{\bullet}CH_2C(CH_3)_2OH$ radical reacts sluggishly, if at all, with the coordination complex and does not interfere with the dynamics of the reactions of {3,4} with the other radicals. Here we employed a similar design (Figure 8a) to measure the rate of reaction between {3,3} and $SO_4^{\bullet-}$ (k_{sr1} in Scheme 1). To avoid thermal oxidation of {3,3} by $S_2O_8^{2-}$ occurring prior to pulse radiolysis in this system, we have used the flow mixing technique illustrated in Figure S1 (Supporting Information).

The transient absorption on a 40 μs time scale following pulse radiolysis shows bleaching at 630 nm and growth at 490 nm (Figure 8b), which is indicative of {3,3} conversion to {3,4}. Extrapolation of the observed rate constant for this change to zero radiation dose, a procedure that corrects for all radical–radical reactions and consumption of {3,3} at higher doses (Figure 8b, inset), yields the bimolecular rate constant $k_{sr1} = 1.6 \times 10^{10}$ M^{-1} s^{-1} at pH 9.2 and μ = 7 mM. Thus, $k_{sr1} \approx k_{sr2}$ are essentially at the diffusion controlled limit, which is not surprising because both reactions are extremely exergonic.

To investigate the reduction of {3,3} by the $(CH_3)_2{}^{\bullet}COH$ radical (k_{ar2} in Scheme 2), we have used pulse radiolysis in a N_2O-saturated solution containing 50 mM 2-PrOH, 20.5 μM {3,3}, and 2 mM NaOH. Under these conditions, all primary radicals from water radiolysis are converted into the alcohol radicals within a microsecond, and the subsequent bleaching of the {3,3} absorption band at 624 nm can only be attributed to the k_{ar2} reaction in Scheme 2. Kinetic analysis of these data yields k_{ar2} =

DOI: 10.1021/acs.jpcb.5b00922
J. Phys. Chem. B 2015, 119, 7749–7760

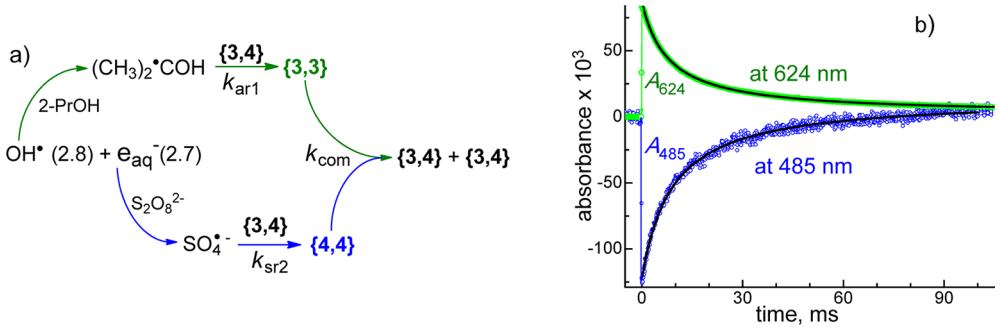

Figure 9. (a) Experimental design for measuring k_{com}. Green and blue arrows represent reactions initiated by the hydroxyl radical and hydrated electron, respectively. Numbers in parentheses represent radiation yields (G-values) for these pathways. (b) Kinetics of the {3,3} + {4,4} comproportionation recorded at 624 nm (green, {3,3} formation and decay) and 485 nm (blue, {3,4} bleaching and recovery). Two Ar-purged solutions, one containing 4 mM 2-PrOH and the other containing 190 μM {3,4}, 19.5 mM $S_2O_8^{2-}$, and 6 mM NaOH, are 1:1 flow-mixed into a flow cell using a remotely controlled syringe pump (Figure S1, Supporting Information) immediately prior to pulse radiolysis. The black lines show fits to the data as described in the text with the k_{com} rate constants 5.4×10^7 M^{-1} s^{-1} (green trace) and 4.7×10^7 M^{-1} s^{-1} (blue trace).

Scheme 3

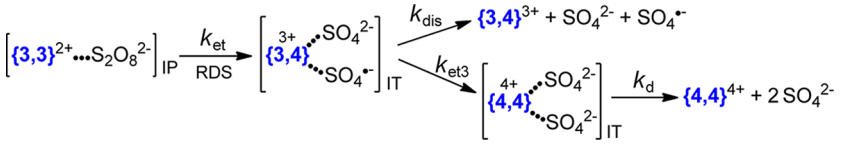

5.1×10^9 M^{-1} s^{-1} (see Figure S4, Supporting Information, for details). In a similarly designed experiment in which 25% stoichiometric excess of $S_2O_8^{2-}$ was added to quantitatively convert {3,3} to {3,4} prior to pulse radiolysis, we have determined $k_{ar1} = 7.2 \times 10^9$ M^{-1} s^{-1} (Figure S5, Supporting Information). Thus, both k_{ar1} and k_{ar2} are nearly diffusion controlled, and our steady-state assumption for $(CH_3)_2{}^{\bullet}COH$ in Scheme 2 is justified.

To evaluate the specific rate of the {3,3} + {4,4} comproportionation (k_{com} in Scheme 1), we have performed pulse radiolysis of a solution containing 95 μM {3,4}, 9.75 mM $S_2O_8^{2-}$, 2 mM 2-PrOH, and 3 mM NaOH. This solution composition was selected to generate nearly equal amounts of the $(CH_3)_2{}^{\bullet}COH$ and $SO_4{}^{\bullet-}$ radicals which, in turn, rapidly convert {3,4} into {3,3} and {4,4}, respectively, as shown in Figure 9a. This conversion is observed in Figure 9b as the appearance of absorption at 624 nm (the {3,3} absorption maximum) and bleaching at 485 nm (the maximum of the {3,4} − {4,4} difference spectrum[30,39]). The observed signal amplitude ratio $A_{485}/A_{624} = 1.44$ is close to the expected value of 1.50 for $\Delta[\{3,3\}] = \Delta[\{4,4\}]$, both the new absorption and bleaching are reversible, and the shapes of kinetic traces at both wavelengths correspond well to second-order processes.

All of these features are consistent with {3,3} + {4,4} comproportionation being observed in Figure 9b. To obtain k_{com}, the integral kinetics prescribed by the comproportionation rate law $d[\{3,4\}]/2dt = -d[\{3,3\}]/dt = -d[\{4,4\}]/dt = k_{com}[\{3,3\}]\cdot[\{4,4\}]$ were fitted to the data using as initial concentrations $[\{3,3\}]_0 = 2.5$ μM and $[\{4,4\}]_0 = 2.4$ μM, values that were determined from the A_{624} and A_{485} amplitudes. From this analysis, we estimate $k_{com} \approx 5 \times 10^7$ M^{-1} s^{-1} at pH 11.5 where all species involved are in their dihydroxy protonation states. This value is sufficiently large to ensure that comproportionation is not rate-limiting under the prevailing conditions of this study: alkaline solutions and μ = 5−50 mM. It follows from Scheme 1 and eq 2 that the steady state concentration of {4,4} is $[\{4,4\}]_{ss} = (1 - \alpha)k_{app}[S_2O_8^{2-}]/k_{com}$, which amounts to a negligible $[\{4,4\}]_{ss} \approx 0.03$ μM under the conditions given in Figure 6.

It is well-known that upon one-electron reduction the $S_2O_8^{2-}$ ion dissociates as in reaction 14. However, it is not known whether this reaction proceeds through a thermally equilibrated intermediate, $S_2O_8{}^{\bullet 3-}$, or whether electron capture by $S_2O_8^{2-}$ is truly dissociative. To probe this issue, we have used pulse radiolysis with sub-nanosecond temporal resolution to compare the transient absorption rise time for formation of the hydrated electron in Ar-purged neat water with that for formation of the $SO_4{}^{\bullet-}$ radical in 2 M $S_2O_8^{2-}$ solution (see Figure S6, Supporting Information, for full details). Although in the latter case the electrons are quantitatively captured by $S_2O_8^{2-}$ within ~0.05 ns, we have observed in both cases the same rise times of ~0.5 ns, which represents the response time of our detection system. This observation clearly indicates that, if the $S_2O_8{}^{\bullet 3-}$ radical exists as the bound thermally equilibrated species, its lifetime does not exceed 0.5 ns.

DISCUSSION

The hypothetical successor complex, $[\{3,4\}^{3+}\cdots S_2O_8{}^{\bullet 3-}]_{SC}$, that would be formed by simple one-electron transfer within the precursor complex ion pair (Scheme 1) is itself a strong ion pair with $Z_AZ_B = -9$ at pH > 4. The stability constant for ion pairing

$$\{3,4\}^{3+} + S_2O_8{}^{\bullet 3-} \underset{k_d}{\overset{k_{-d}}{\rightleftharpoons}} [\{3,4\}^{3+}\cdots S_2O_8{}^{\bullet 3-}]_{SC}$$

estimated from eqs 6 and 7, is $K_{SC} = k_{-d}/k_d \sim 10^3$ M^{-1} at $\mu = 0.02$ M, an ionicity that is typical for this study. This large K_{SC} and the very short measured lifetime of the $S_2O_8{}^{\bullet 3-}$ radical (<0.5 ns, Figure S6, Supporting Information) ensure that O−O bond cleavage will occur within the successor complex. This follows because the rate constant for ion association cannot be greater than the diffusion-controlled limit of $k_{-d} \sim 10^{10}$ M^{-1} s^{-1}, so that the ion pair lifetime must exceed $1/k_d = K_{SC}/k_{-d} \sim 100$ ns, which is at least 200-fold greater than the $S_2O_8{}^{\bullet 3-}$ lifetime. We can thus

DOI: 10.1021/acs.jpcb.5b00922
J. Phys. Chem. B 2015, 119, 7749−7760

suggest a more detailed description of the rate-determining step in Scheme 1, which is shown in Scheme 3.

Here, electron transfer is viewed as dissociative (DET), involving rupture of the O−O bond in the transition state followed by formation of the ion triple, in which all three ions are free to move (translationally and rotationally) relative to each other. Similar DET mechanisms have been invoked for oxidations by both peroxydisulfate ion[5,9,10] and organic peroxides.[41] Because the k_{et} step is rate determining, the partitioning between the one-electron k_{et1} and two-electron k_{et2} oxidation pathways is identified as the competition between two very rapid processes, those of $SO_4^{\bullet-}$ radical escape from the ion triple and intratriple oxidation of {3,4} by $SO_4^{\bullet-}$. In terms of notations in Schemes 1 and 3, $k_{et1} = k_{et}k_{dis}/(k_{dis} + k_{et3})$ and $k_{et2} = k_{et}k_{et3}/(k_{dis} + k_{et3})$, and our radical scavenging results with 2-PrOH indicate that $SO_4^{\bullet-}$ escapes the ion triple with ∼25% probability.

At this point, it is instructive to consider the energetics of blue dimer oxidation by peroxydisulfate, which is illustrated by the E_h−pH predominance diagram in Figure 10. Notably, the {4,4} domain at neutral and alkaline pH and the {4,5} domain at acidic pH are absent due to instabilities of these oxidation states toward disproportionation

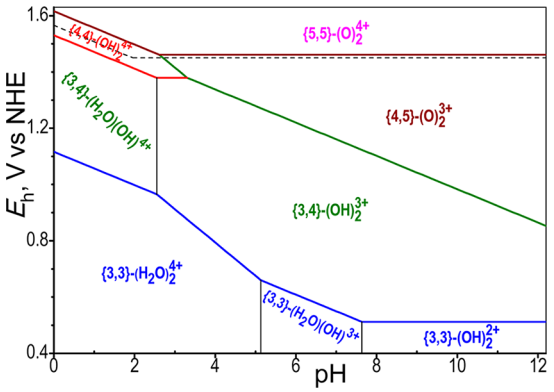

Figure 10. E_h−pH predominance diagram for blue dimer species constructed using reduction potentials and pK_a corrected to zero ionic strength, as shown in Tables S1 and S2 (Supporting Information). The {4,4} species is doubly deprotonated,[27,30] and the {4,5} and {5,5} species are fully deprotonated[27,30,42] over the entire pH range. The dashed line corresponds to the one-electron reduction potential of peroxydisulfate: $E^0(S_2O_8^{2-}/SO_4^{\bullet-}, SO_4^{2-})$ = 1.45 V and p$K_a(HSO_4^-)$ = 1.96. A predominance diagram based upon data that are not corrected for ionic strength is shown in Figure S7 (Supporting Information).

$$\{4,4\}\text{-}(OH)_2 + \{4,4\}\text{-}(OH)_2 = \{4,5\}\text{-}(O)_2 + \{3,4\}\text{-}(OH)_2 + 2H^+ \quad \Delta G^0 < 0 \quad \text{at} \quad \text{pH} > 3.3 \tag{17}$$

$$\{4,5\}\text{-}(O)_2 + \{4,5\}\text{-}(O)_2 + 2H^+ = \{5,5\}\text{-}(O)_2 + \{4,4\}\text{-}(OH)_2 \quad \Delta G^0 < 0 \quad \text{at} \quad \text{pH} < 2.6 \tag{18}$$

As a result, all four oxidation states are found only in a narrow pH range, and the very existence of this range is a subject to knowing the differences between reduction potentials of {4,4}, {4,5}, and {5,5} to better than 0.04 V.

It is clear from Figure 10 that the rate determining k_{et} step becomes significantly more favorable with increasing medium pH, which is undoubtedly responsible for the rate−pH dependence in Figure 6. The relationship between the overall standard reaction free energy (ΔG^0)

$$\Delta G^0 = E^0(\{3,4\}/\{3,3\}) - E^0(S_2O_8^{2-}/SO_4^{\bullet-}, SO_4^{2-}) \tag{19}$$

and that of the one-electron transfer step ($\Delta G^{0\prime}$) are schematically shown in Figure 11a and given by

$$\Delta G^{0\prime} = \Delta G^0 + RT \ln \frac{K_{IP}^0}{K_{IT}^0} \tag{20}$$

(For a nondissociative electron transfer when both reactants and products are ion pairs, this equation reduces to the more familiar form $\Delta G^{0\prime} = G^0 + W_p - W_r$, where W_p and W_r are the electrostatic work for ion pairing of products and reactants, respectively.) The value of K_{IP}^0 can be obtained from eqs 6 and 7 (with $\mu = 0$), and a procedure for evaluating K_{IT}^0 is developed in Figure S8 (Supporting Information).

In Figure 11b, values of k_{et} for oxidation of {3,3} in its three protonation states are plotted against their corresponding $\Delta G^{0\prime}$ calculated under the assumption that the nascent {3,4} products retain the reactant's protonation states. In other words, the k_{et} step involves breakage of only the peroxo bond in $S_2O_8^{2-}$ and pH equilibration of {3,4} with the medium, if any, occurs later (see the following paragraph for additional discussion). For comparison, analogous plots for two sets of complexes that contain no coordinated water are also shown in Figure 11b (see Table S3, Supporting Information, for full details). Collectively, the three plots span about 1 eV in $\Delta G^{0\prime}$ and 8 orders of magnitude in k_{et}, and in each case, a good linear dependence of the form $\ln(k_{et}) = a + b\Delta G^{0\prime}$ is observed. Because $k_{et} = \sigma(kT/h)\exp(-\Delta G^{\#}/RT)$, where σ combines the steric factor and electronic transmission coefficient, we write

$$\Delta G^{\#} = RT\left[\ln\left(\sigma\frac{kT}{h}\right) - a\right] - RTb\Delta G^{0\prime} \tag{21}$$

The $-RTb$ slopes in this dependence are nearly identical for all three series at 0.39 (BD series), 0.44 (G series), and 0.39 (R series).

The very similar linear free energy correlations for reaction of the "blue dimer" and other complex ions (Figure 11b) support the assumed reaction model (Scheme 3). One notes that the alkaline pathway involves simple electron transfer, whereas net oxidation by the other pathways leads to release of one to two protons. Coupling of proton transfer to a solvent water molecule with electron transfer to $S_2O_8^{2-}$ (PCET), if it existed, would be expected to substantially increase $\Delta G^{0\prime}$ values for the neutral and acid pathways relative to the alkaline pathway and to shift points 2 and 3 in Figure 11b to the right. This is not evident in the figure, where the slope for the BD series is nearly identical to the other sets of data, and the absolute values of k_{et} are in accord with expectations from other polypyridine-ligated complexes (series G) that undergo simple one-electron transfer. We therefore conclude that PCET is not an important factor in these reactions.

According to a theoretical model developed by Savéant,[43,44] free energy correlations for dissociative electron transfer should have the same quadratic form as that prescribed by Marcus theory, namely,

DOI: 10.1021/acs.jpcb.5b00922
J. Phys. Chem. B 2015, 119, 7749−7760

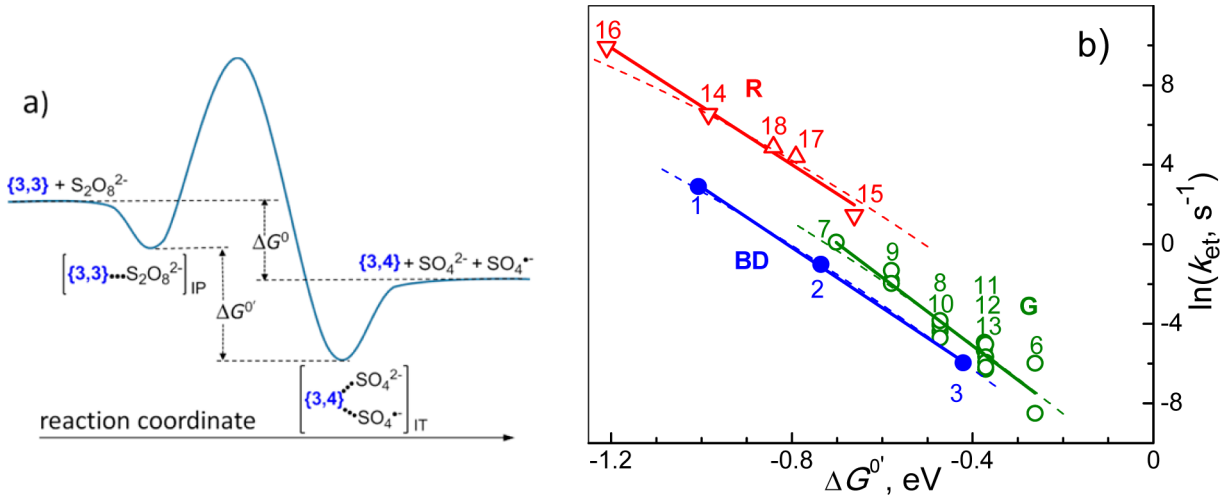

Figure 11. (a) Schematic representation of the free energy profile for a dissociative electron transfer. (b) Dependencies of k_{et} upon $\Delta G^{0'}$ (see Table S3, Supporting Information, for numerical data, detail, and references). Series BD (solid blue circles): blue dimer species {**3,3**}-$(OH)_2$ (1), {**3,3**}-$(H_2O)(OH)$ (2), and {**3,3**}-$(H_2O)_2$ (3). Series G (open green circles): $Ru(bpy)_3^{2+}$, $Os(bpy)_3^{2+}$, and FeL_n^{2+} polypyridine- and phenanthroline-based complex ions. Series R (open red triangles): $Ru(NH_3)_5$-based mononuclear (down triangles) and pyrazine-bridged binuclear (up triangles) ions. Numerical labels match entries in Table S3 (Supporting Information). The solid lines show linear fits: $-(12.3 \pm 0.3) - (15.2 \pm 0.4\ eV^{-1})\Delta G^{0'}$ (BD series), $-(12.0 \pm 0.6) - (17.2 \pm 1.3\ eV^{-1})\Delta G^{0'}$ (G series), and $-(7.7 \pm 1.0) - (14.7 \pm 1.1\ eV^{-1})\Delta G^{0'}$ (R series). The dashed lines show fits to the data using $k_{et} = (\sigma kT/h)\exp(-\Delta G^{\#}/RT)$ and eq 22 with $\sigma = 10^{-6}$ for all series and $\lambda = 3.0$ (BD series), 2.9 (G series), and 2.5 eV (R series).

$$\Delta G^{\#} = \frac{\lambda}{4}\left(1 + \frac{G^{0'}}{\lambda}\right)^2 = \frac{\lambda}{4} + \frac{1}{2}\left(1 + \frac{\Delta G^{0'}}{2\lambda}\right)\Delta G^{0'} \qquad (22)$$

where λ includes the enthalpy of the dissociating bond (in our case, the BDE of the O−O bond in $S_2O_8^{2-}$) and the reorganization free energy (λ_0), so that λ = BDE + λ_0. Although this BDE is unknown, it can easily contribute in excess of 2 eV (e.g., BDE = 2.2 eV for the HO−OH bond).[45] The contribution to λ from reorganization is also expected to be substantial, as the dissociative electron transfer involves major spatial redistribution of charge. Thus, we should expect that $\lambda \gg |\Delta G^{0'}|/2$ and for eq 22 to appear nearly linear over a sufficiently small $\Delta G^{0'}$ range. This approximation predicts a slope that is slightly less than 0.5, which is consistent with the $-RTb$ slope of about 0.4 derived from the data and eq 21.

To compare predictions of eq 22 with the data in Figure 11b, we need to have at least an estimate for the value of σ, and this information can be obtained from the entropy of activation. A curious feature of the peroxydisulfate oxidation of {**3,3**}-$(OH)_2$ is that, despite a bond dissociation in the transition state, this reaction exhibits significantly negative apparent activation entropy ($\Delta S_{app}^{\#} \approx -21$ e.u.), as derived from the temperature dependence in Figure 5. However, this appears to be a common trend for peroxydisulfate oxidations. The activation data for a series of ML_n^{2+} polypyridine- and phenanthroline-based complex ions compiled in Table S4 (Supporting Information) show that $\Delta S_{app}^{\#}$ values for their oxidations by $S_2O_8^{2-}$ average about −23 e.u. Although noted previously,[1,2,46] these negative activation entropies have not been adequately explained. Here, we shall attempt a semiquantitative interpretation of this feature.

Considering the reaction mechanism that leads to $k_{app} = 2\sigma(kT/h)K_{IP}k_{et}$, we write $\Delta S_{app}^{\#} = R\ln 2\sigma + \Delta_{IP}S + \Delta_{et}S^{\#}$. In terms of the model in Figure 11, using eqs 20 and 22, and assuming that $\lambda \gg |\Delta G^{0'}|$ and is temperature-independent, we derive

$$\Delta S_{app}^{\#} \approx R\ln 2\sigma + \frac{1}{2}(\Delta S^0 + \Delta_{IT}S + \Delta_{IP}S) \qquad (23)$$

where ΔS^0, $\Delta_{IP}S$, and $\Delta_{IT}S$ are entropies of the overall reaction, reactant ion pairing, and product ion tripling, respectively. It has been shown that the entropy changes upon one-electron oxidation of trisbipyridine and trisphenanthroline complexes of divalent Ru and Fe are typically small; e.g., $S_{ox}^0 - S_{red}^0$ is about 2 e.u. for the $Fe(4,4'\text{-}Me_2\text{-}bpy)_3^{2+/3+}$ pair,[1] and for the present purposes, we will use this value. Although the entropy of $SO_4^{\bullet-}$ is unknown, it should be nearly equal to that of HSO_4^-. Using tabulated data for this anion, SO_4^{2-}, and $S_2O_8^{2-}$,[47] we estimate $\Delta S^0 \approx -20$ e.u. The values of $\Delta_{IP}S$ and $\Delta_{IT}S$ evaluated at $\mu = 0$ from eq 9 and the model in Figure S8 (Supporting Information) are both substantially positive at about 9 and 17 e.u., respectively, for all complexes in Table S4 (Supporting Information). Thus, the second term in eq 23 is positive and small at about 4 e.u., and to account for the average observed $\Delta S_{app}^{\#} \approx -23$ e.u., we must assume σ to be of the order of 10^{-6}. In mechanistic terms, this low number suggests a high degree of nonadiabaticity for the electron transfer step, which is likely associated with poor electronic coupling between the metal ion and $S_2O_8^{2-}$.

Although the degree of nonadiabaticity for oxidation by $S_2O_8^{2-}$ may vary from series to series and even within a series in Figure 11b, for illustrative purposes, we have set $\sigma = 10^{-6}$ and applied the unabridged eq 22 to the data. The dashed lines in Figure 11b show that this model accounts fairly well for the data provided that λ is sufficiently large: 3.0 (BD series), 2.9 (G series), and 2.5 eV (R series). Comparing eq 21 with eq 22 at $\lambda \gg |\Delta G^{0'}|/2$, we identify $\lambda/4$ as $RT[\ln(\sigma kT/h) - a]$ (that is, as the activation free energy for the reaction at zero driving force) and, with $\sigma = 10^{-6}$, we calculate λ = 2.9 (BD series), 2.8 (G series), and 2.4 eV (R series), which are essentially the same as the λ values obtained from the quadratic fit. Thus, our suggestions of strong nonadiabaticity and large reorganization energy are consistent with the observed rates and activation parameters. The clearly noticeable offsets, especially for the R series, in Figure 11b are not readily explicable within the simple model used here and may require invoking specific $S_2O_8^{2-}$−ligand interactions that modulate K_{IP}, σ, or both. One such model proposed by Haim postulates H-bond formation between three adjacent coordi-

DOI: 10.1021/acs.jpcb.5b00922
J. Phys. Chem. B 2015, 119, 7749−7760

nated NH_3 molecules and three cofacially aligned oxygen atoms of a SO_3 moiety of peroxydisulfate.[8]

As shown in the E_h–pH predominance diagrams (Figure 10 and Figure S7, Supporting Information), persulfate oxidation of {3,3} to higher oxidation states ({4,5} and {5,5}) through a mechanism similar to that in Scheme 1 is thermodynamically limited in acid solutions but not in alkaline media, where all oxidation states of the dimer are accessible. Using the linear dependence in Figure 11 and eqs 6 and 7, we estimate (Table S3, Supporting Information) the apparent rate constant for further oxidation of {3,4} in neutral and alkaline solutions

$$\{\mathbf{3,4}\}\text{-}(OH)_2 + S_2O_8^{2-} \rightarrow (1-\alpha)(\{\mathbf{4,5}\}\text{-}(O)_2 + 2SO_4^{2-} + 2H^+) + \alpha(\{\mathbf{4,4}\}\text{-}(OH)_2 + SO_4^{\bullet-}) \quad (24)$$

as $k_{app} = 2K_{IP}k_{et} \approx 3 \times 10^{-3}\ M^{-1}\ s^{-1}$ at $\mu = 0.03$ M (10 mM $K_2S_2O_8$) and the {3,4} half-life under these conditions as ~8 h. Similarly, for oxidation of {4,5}

$$\{\mathbf{4,5}\}\text{-}(O)_2 + S_2O_8^{2-} \rightarrow \{\mathbf{5,5}\}\text{-}(O)_2 + SO_4^{2-} + SO_4^{\bullet-} \quad (25)$$

we estimate $k_{app} = 2K_{IP}k_{et} \approx 9 \times 10^{-4}\ M^{-1}\ s^{-1}$ ($\mu = 0.03$ M) and $t_{1/2}$ ~27 h in 10 mM $S_2O_8^{2-}$. Such slow rates render reactions 24 and 25 to be of little utility, particularly in light of the previously detected instability of {4,5} toward nucleophilic attack by the hydroxide ion on a bipyridine ligand that initiates its deep oxidative destruction with attendant consumption of numerous {4,5} ions.[48] It is thus not surprising that, although access to {5,5} should lead to dimer-catalyzed water oxidation by peroxydisulfate,[27,49] incubation of an anaerobic alkaline solution containing 69 μM {3,4} and 10 mM $S_2O_8^{2-}$ for up to 5 h did not yield any detectable O_2 formation, as determined using a sensitive fluorescence technique.

The near-diffusion rate constants measured for reaction of $SO_4^{\bullet-}$ with {3,3} and {3,4} indicate that this radical is a highly reactive and indiscriminant oxidant. In reactions where it is generated (for example, photosensitized water oxidation systems using $S_2O_8^{2-}$ as a terminal electron acceptor),[11−24] $SO_4^{\bullet-}$ may strongly influence the overall performance of the system. In these cases, in addition to oxidizing the photosensitizer, the radical may react directly with the water oxidation catalyst to generate the higher oxidation states that are either catalytically active or engage in degradative reactions that lead to modification or loss of catalytic activity. A case in point is water photooxidation by the $S_2O_8^{2-}$/$Ru(bpy)_3^{2+}$/"blue dimer" system, where the potentials for photogenerated $Ru(bpy)_3^{3+}$ ($E_{1/2}(Ru^{III/II})$ = 1.27 V) and $Ru(dmb)_3^{2+}$ ($E_{1/2}$ = 1.11 V; dmb ≡ 4,4′-dimethyl-2,2′-bipyridine) are insufficient to drive oxidation of {3,3} to the catalytically active {5,5} state (Figure 10), yet O_2 evolution was observed.[14] In contrast, thermal reaction of {3,3} with a large excess of chemically prepared $Ru(bpy)_3^{3+}$ did not lead to detectable O_2 accumulation, implicating $SO_4^{\bullet-}$ in the formation of {5,5}. This conclusion is supported by studies demonstrating a marked dependence of rates of photoinitiated O_2 evolution upon the sensitizer reduction potential[50] and markedly increased transient state levels of {5,5} (as determined by resonance Raman spectroscopy) when a more strongly oxidizing homologue ($Ru(dcb)_2(bpy)^{2+}$, $E_{1/2}$ = 1.51 V; dcb ≡ 4,4′-dicarbethoxy-2,2′-bipyridine) was used as a photosensitizer.[14,28] Similar conclusions have recently been drawn by Bonchio and co-workers, who demonstrated by transient spectroscopy that photochemical yields of $Ru(bpy)_3^{3+}$ formed by reaction with $S_2O_8^{2-}$ were diminished in the presence of a Co_4–cubane water oxidation catalyst, implying that direct oxidation of the Co_4 catalyst by $SO_4^{\bullet-}$ competed with oxidation of $Ru(bpy)_3^{2+}$.[22] These studies clearly demonstrate that accurate mechanistic interpretation of chemical and photocatalytic reactions utilizing $S_2O_8^{2-}$ as a terminal oxidant will require quantification of the fate of the $SO_4^{\bullet-}$ radical that is generated as a reactive intermediate.

■ ASSOCIATED CONTENT

Supporting Information

Evaluation of $S_2O_8^{2-}$ and {3,3} radii. Experimental setup for performing pulse radiolysis with flow premixing. Redox titration determination of stoichiometry of the {3,3} oxidation by $S_2O_8^{2-}$. Kinetics of {3,3} oxidation at various medium pH. Pulse radiolysis determinations of the rate constants for the {3,3} and {3,4} reactions with $(CH_3)_2{}^{\bullet}COH$ and the upper limit for the $S_2O_8^{\bullet 3-}$ radical lifetime. E_h–pH predominance diagram for blue dimer species computed using raw literature data uncorrected for ionic strength. A procedure for evaluating the thermodynamics of ion tripling. Tables containing pK_a and reduction potentials of blue dimer species, data for correlating k_{et} with $\Delta G^{0'}$, and activation parameters for complex ion oxidations by $S_2O_8^{2-}$. This material is available free of charge via the Internet at http://pubs.acs.org.

■ AUTHOR INFORMATION

Corresponding Author

*E-mail: lymar@bnl.gov. Phone: (631) 344-4333.

Notes

The authors declare no competing financial interest.

■ ACKNOWLEDGMENTS

We thank John Miller for help with picosecond pulse radiolysis, Dmitry Polansky for assistance with the oxygen evolution studies, and Norman Sutin for valuable discussions. This work and use of the 2 MeV electron Van de Graaff and LEAF Facility of the Brookhaven National Laboratory (BNL) Accelerator Center for Energy Research was supported by the US Department of Energy, Office of Science, Office of Basic Energy Sciences, Division of Chemical Sciences, Geosciences and Biosciences, under contracts DE-AC02-98CH10886 and DE-SC0012704 (at BNL) and through grant DE-FG02-06ER15820 (to Washington State University). M.D.R. received scholastic support from HHMI grant 52005883 (administered by Oregon State University).

■ REFERENCES

(1) Irvine, D. H. The Kinetics of the Oxidation of Some Bipyridyl and Phenanthroline Complex Ions by the Peroxydisulphate Ion in Aqueous Solution. *J. Chem. Soc.* **1959**, 2977−2981.

(2) Burgess, J.; Prince, R. H. Peroxydisulphate Oxidation of Iron(II) Complexes of Substituted 1,10-Phenanthrolines and Related Compounds. *J. Chem. Soc. A* **1966**, 1772−1775.

(3) Burgess, J.; Prince, R. H. Kinetics of Reaction of Peroxodisulphate with the 5-Nitro-, 3-Sulphonato- and 5-Sulphonato-Substituted Derivatives of the Tris-(1,10-Phenanthroline)iron(II) Cation in Aqueous Solution. *J. Chem. Soc. A* **1970**, 2111−2113.

(4) Yeh, A.; Haim, A. Aqueous Solution Chemistry of μ-Pyrazinepentaammineruthenium(II,III) Pentacyanoferrate(II,III): Formation, Redox Reactions, and Intervalence Properties. *J. Am. Chem. Soc.* **1985**, *107*, 369−376.

DOI: 10.1021/acs.jpcb.5b00922
J. Phys. Chem. B 2015, 119, 7749−7760

(5) Fürholz, U.; Haim, A. Kinetics and Mechanisms of the Reactions of Mononuclear and Binuclear Ruthenium(II) Ammine Complexes with Peroxydisulfate. *Inorg. Chem.* **1987**, *26*, 3243−3248.
(6) Olabe, J. A.; Haim, A. An Example of Intramolecular Electron-Transfer Assistance in a Bimolecular Redox Reaction: Peroxydisulfate Oxidation of (μ-1,2-Bis(4-pyridyl)ethane)pentaammineruthenium(III) Pentacyanoferrate(II) via Its Electronic Isomer. *Inorg. Chem.* **1989**, *28*, 3277−3278.
(7) Parise, A. R.; Baraldo, L. M.; Olabe, J. A. Electronic Structure and Substitution and Redox Reactivity of Imidazolate-Bridged Complexes of Pentacyanoferrate and Pentaammineruthenium. *Inorg. Chem.* **1996**, *35*, 5080−5086.
(8) Haim, A. Redox Reactions of Binuclear Complexes of Ruthenium and Iron. *Adv. Chem. Ser.* **1997**, *253*, 239−254.
(9) Kläning, U.; Byberg, J. R.; Daasbjerg, K.; Sehested, K.; Appelman, E. H. Electron Transfer Reactions of Peroxydisulfate and Fluoroxysulfate Reactions with the Cyanide Complexes $M(CN)_n^{4-}$ (M=Fe(II), Ru(II), Os(II), Mo(IV), and W(IV). *J. Phys. Chem. A* **2007**, *111*, 1419−1425.
(10) Lewandowska-Andralojc, A.; Polyansky, D. E. Mechanism of the Quenching of the Tris(bipyridine)ruthenium(II) Emission by Persulfate: Implications for Photoinduced Oxidation Reactions. *J. Phys. Chem. A* **2013**, *117*, 10311−10319.
(11) Rotzinger, F. P.; Munavalli, S.; Comte, P.; Hurst, J. K.; Grätzel, M.; Pern, F. J.; Frank, A. J. A Molecular Water-Oxidation Catalyst Derived from Ruthenium Diaqua Bis(2,2′-Bipyridyl-5,5′-Dicarboxylic Acid). *J. Am. Chem. Soc.* **1987**, *109*, 6619−6626.
(12) Comte, P.; Nazeeruddin, M. K.; Rotzinger, F. P.; Frank, A. J.; Grätzel, M. Artificial Analogs of the Oxygen-Evolving Complex in Photosynthesis: the Oxo-Bridged Ruthenium Dimer $L_2(H_2O)Ru^{III}$-O-$Ru^{III}(H_2O)L_2$, L = 2,2′-Bipyridyl-4,4′-Dicarboxylate. *J. Mol. Catal.* **1989**, *52*, 63−84.
(13) Gerasimov, O. V.; Lymar, S. V.; Parmon, V. N. Water Photo-Oxidation Sensitized by Zinc(II) Meso-Tetrakis(N-Methyl-4-Pyridyl)-Porphine. *J. Photochem. Photobiol., A* **1991**, *56*, 275−285.
(14) Cape, J. L.; Hurst, J. K. Detection and Mechanistic Relevance of Transient Ligand Radicals Formed During $[Ru(bpy)_2(OH_2)]_2O^{4+}$-Catalyzed Water Oxidation. *J. Am. Chem. Soc.* **2008**, *130*, 827−829.
(15) Duan, L.; Xu, Y.; Zhang, P.; Wang, M.; Sun, L. Visible Light-Driven Water Oxidation by a Molecular Ruthenium Catalyst in Homogeneous System. *Inorg. Chem.* **2010**, *49*, 209−215.
(16) Xu, Y.; Fischer, A.; Duan, L.; Tong, L.; Gabrielsson, E.; Åkermark, B.; Sun, L. Chemical and Light-Driven Oxidation of Water Catalyzed by an Efficient Dinuclear Ruthenium Complex. *Angew. Chem., Int. Ed.* **2010**, *49*, 8934−8937.
(17) Xu, Y.; Duan, L.; Tong, L.; Åkermark, B.; Sun, L. Visible Light-Driven Water Oxidation Catalyzed by a Highly Efficient Dinuclear Ruthenium Complex. *Chem. Commun.* **2010**, *46*, 6506−6508.
(18) Duan, L.; Xu, Y.; Tong, L.; Sun, L. Ce^{IV}- and Light-Driven Water Oxidation by $[Ru(terpy)(pic)_3]^{2+}$ Analogues: Catalytic and Mechanistic Studies. *ChemSusChem* **2011**, *4*, 238−244.
(19) Huang, Z.; Luo, Z.; Geletii, Y. V.; Vickers, J. W.; Yin, Q.; Wu, D.; Hou, Y.; Ding, Y.; Song, J.; Musaev, D. G.; Hill, C. L.; Lian, T. Efficient Light-Driven Carbon-Free Cobalt-Based Molecular Catalyst for Water Oxidation. *J. Am. Chem. Soc.* **2011**, *133*, 2068−2071.
(20) Hong, D.; Jung, J.; Park, J.; Yamada, Y.; Suenobu, T.; Lee, Y.-M.; Nam, W.; Fukuzumi, S. Water-Soluble Mononuclear Cobalt Complexes with Organic Ligands Acting as Precatalysts for Efficient Photocatalytic Water Oxidation. *Energy Environ. Sci.* **2012**, *5*, 7606−7616.
(21) Berardi, S.; La Ganga, G.; Natali, M.; Bazzan, I.; Puntoriero, F.; Sartorel, A.; Scandola, F.; Campagna, S.; Bonchio, M. Photocatalytic Water Oxidation: Tuning Light-Induced Electron Transfer by Molecular Co_4O_4 Cores. *J. Am. Chem. Soc.* **2012**, *134*, 11104−11107.
(22) La Ganga, G.; Puntoriero, F.; Campagna, S.; Bazzan, I.; Berardi, S.; Bonchio, M.; Sartorel, A.; Natali, M.; Scandola, F. Light-Driven Water Oxidation with a Molecular Tetra-Cobalt(III) Cubane Cluster. *Faraday Discuss.* **2012**, *155*, 177−190.
(23) Hong, D.; Yamada, Y.; Nagatomi, T.; Takai, Y.; Fukuzumi, S. Catalysis of Nickel Ferrite for Photocatalytic Water Oxidation Using $[Ru(bpy)_3]^{2+}$ and $S_2O_8^{2-}$. *J. Am. Chem. Soc.* **2012**, *134*, 19572−19575.
(24) Zhu, G.; Glass, E. N.; Zhao, C.; Lv, H.; Vickers, J. W.; Geletii, Y. V.; Musaev, D. G.; Song, J.; Hill, C. L. A Nickel Containing Polyoxometalate Water Oxidation Catalyst. *Dalton Trans.* **2012**, *41*, 13043−13049.
(25) Armstrong, D. A.; Huie, R. E.; Lymar, S.; Koppenol, W. H.; Merényi, G.; Neta, P.; Stanbury, D. M.; Steenken, S.; Wardman, P. Standard Electrode Potentials Involving Radicals in Aqueous Solution: Inorganic Radicals. *BioInorg. React. Mech.* **2013**, *9*, 59−61.
(26) Gilbert, J. A.; Geselowitz, D.; Meyer, T. J. Redox Properties of the Oxo-Bridged Osmium Dimer $[(bpy)_2(OH_2)Os^{III}OOs^{IV}(OH_2)(bpy)_2]^{4+}$. Implications for the Oxidation of Water to Oxygen. *J. Am. Chem. Soc.* **1986**, *108*, 1493−1501.
(27) Yamada, H.; Hurst, J. K. Resonance Raman, Optical Spectroscopic, and EPR Characterization of the Higher Oxidation States of the Water Oxidation Catalyst, *cis,cis*-$[(bpy)_2Ru(OH_2)]_2O^{4+}$. *J. Am. Chem. Soc.* **2000**, *122*, 5303−5311.
(28) Hurst, J. K.; Cape, J. L.; Clark, A. E.; Das, S.; Qin, C. Mechanisms of Water Oxidation Catalyzed by Ruthenium Diimine Complexes. *Inorg. Chem.* **2008**, *47*, 1753−1764.
(29) Gilbert, J. A.; Eggleston, D. S.; Murphy, W. R.; Geselowitz, D. A.; Gersten, S. W.; Hodgson, D. J.; Meyer, T. J. Structure and Redox Properties of the Water-Oxidation Catalyst $[(bpy)_2(OH_2)RuORu(OH_2)(bpy)_2]^{4+}$. *J. Am. Chem. Soc.* **1985**, *107*, 3855−3864.
(30) Cape, J. L.; Lymar, S. V.; Lightbody, T.; Hurst, J. K. Characterization of Intermediary Redox States of the Water Oxidation Catalyst, $[Ru(bpy)_2OH_2)]_2O^{4+}$. *Inorg. Chem.* **2009**, *48*, 4400−4410.
(31) Debye, P. Reaction Rates in Ionic Solutions. *J. Electrochem. Soc.* **1942**, *82*, 265−272.
(32) Sutin, N. Theory of Electron Transfer Reactions: Insights and Hindsights. *Prog. Inorg. Chem.* **1983**, *30*, 441−498.
(33) Marcus, R. A.; Sutin, N. Electron Transfers in Chemistry and Biology. *Biochim. Biophys. Acta* **1985**, *811*, 265−322.
(34) Fuoss, R. M. Ionic Association. III. The Equilibrium between Ion Pairs and Free Ions. *J. Am. Chem. Soc.* **1958**, *80*, 5059−5061.
(35) Allan, D. R. Sodium Peroxodisulfate. *Acta Crystallogr., Sect. E* **2006**, *62*, i44−i46.
(36) Fernández, D. P.; Mulev, Y.; Goodwin, A. R. H.; Sengers, J. M. H. L. A Database for the Static Dielectric Constant of Water and Steam. *J. Phys. Chem. Ref. Data* **1995**, *24*, 33−70.
(37) Neta, P.; Huie, R. E.; Ross, A. B. Rate Constants for Reactions of Inorganic Radicals in Aqueous Solution. *J. Phys. Chem. Ref. Data* **1988**, *17*, 1027−1284.
(38) Schwarz, H. A.; Dodson, R. W. Reduction Potentials of CO_2^- and the Acohol Radicals. *J. Phys. Chem.* **1989**, *93*, 409−414.
(39) Polyansky, D. E.; Hurst, J. K.; Lymar, S. V. Application of Pulse Radiolysis to Mechanistic Investigations of Water Oxidation Catalysis. *Eur. J. Inorg. Chem.* **2014**, 619−634.
(40) Buxton, G. V.; Greenstock, C. L.; Helman, W. P.; Ross, A. B. Critical Review of Rate Constants for Reactions of Hydrated Electrons, Hydrogen Atoms and Hydroxyl Radicals ($\cdot OH/\cdot O^-$) in Aqueous Solution. *J. Phys. Chem. Ref. Data* **1988**, *17*, 513−886.
(41) Donkers, R. L.; Maran, F.; Wayner, D. D. M.; Workentin, M. S. Kinetics of the Reduction of Dialkyl Peroxides. New Insights into the Dynamics of Dissociative Electron Transfer. *J. Am. Chem. Soc.* **1999**, *121*, 7239−7248 and references cited therein..
(42) Yamada, H.; Koike, T.; Hurst, J. K. Water Exchange Rates in the Diruthenium μ-Oxo Ion *cis,cis*-$[(bpy)_2Ru(OH_2)]_2O^{4+}$. *J. Am. Chem. Soc.* **2001**, *123*, 12775−12780.
(43) Savéant, J. M. A Simple Model for the Kinetics of Dissociative Electron Transfer in Polar Solvents. Application to the Homogeneous and Heterogeneous Reduction of Alkyl Halides. *J. Am. Chem. Soc.* **1987**, *109*, 6788−6795.
(44) Savéant, J. M. Electron Transfer, Bond Breaking, and Bond Formation. *Acc. Chem. Res.* **1993**, *26*, 455−461.
(45) Luo, Y.-R. *Comprehensive Handbook of Chemical Bond Energies*; CRC Press: Boca Raton, FL, 2007.

DOI: 10.1021/acs.jpcb.5b00922
J. Phys. Chem. B 2015, 119, 7749−7760

(46) Raman, S.; Brubaker, C. H., Jr The Kinetics of the Oxidation of Substituted 2,2′-Bipyridine and 1,10-Phenanthroline Complexes of Iron(II) with Peroxydisulfate Ion. *J. Inorg. Nucl. Chem.* **1969**, *31*, 1091−1099.
(47) Wagman, D. D.; Evans, W. H.; Parker, V. B.; Schumm, R. H.; Halow, I.; Bailey, S. M.; Churney, K. L.; Nuttall, R. L. The NBS Tables of Chemical Thermodynamic Properties. *J. Phys. Chem. Ref. Data* **1982**, *11*, Suppl. 2.
(48) Kutner, W.; Gilbert, J. A.; Tomaszewski, A.; Meyer, T. J.; Murray, R. W. Stability and Electrocatalytic Activity of the Oxo-Bridged Dimer $[(bpy)_2(H_2O)RuORu(OH_2)(bpy)_2]^{4+}$ in Basic Solutions. *J. Electroanal. Chem.* **1986**, *205*, 185−207.
(49) Yamada, H.; Siems, W. F.; Koike, T.; Hurst, J. K. Mechanisms of Water Oxidation Catalyzed by the *cis*,*cis*-$[(bpy)_2Ru(OH_2)]_2O^{4+}$ Ion. *J. Am. Chem. Soc.* **2004**, *126*, 9786−9795.
(50) Cape, J. L.; Hurst, J. K. Unpublished Observations.

DOI: 10.1021/acs.jpcb.5b00922
J. Phys. Chem. B 2015, 119, 7749−7760